Volume 34, issue 9, September 2011

ISSN 0309-1708

ELSEVIER

Advances *in* Water Resources

Special Issue on
Computational Challenges
in the Solution of Water
Resources Problems
Guest Editors
Mark Bakker
Matthew W. Farthing
Christopher E. Kees
Carol S. Woodward

Available online at www.sciencedirect.com
SciVerse ScienceDirect

The GeoClaw software for depth-averaged flows with adaptive refinement

Marsha J. Berger, David L. George *, Randall J. LeVeque, Kyle T. Mandli

Courant Institute of Mathematical Sciences, 251 Mercer St., New York, USA
Cascades Volcano Observatory, US Geological Survey, 1300 SE Cardinal Ct. #100, Vancouver, WA 98683, USA
Department of Applied Mathematics, University of Washington, Box 352420, Seattle, WA 98195-2420, USA

ARTICLE INFO

ABSTRACT

Many geophysical flow or wave propagation problems can be modeled with two-dimensional depth-averaged equations, of which the shallow water equations are the simplest example. We describe the GeoClaw software that has been designed to solve problems of this nature, consisting of open source Fortran programs together with Python tools for the user interface and flow visualization. This software uses high-resolution shock-capturing finite volume methods on logically rectangular grids, including latitude–longitude grids on the sphere. Dry states are handled automatically to model inundation. The code incorporates adaptive mesh refinement to allow the efficient solution of large-scale geophysical problems. Examples are given illustrating its use for modeling tsunamis and dam-break flooding problems. Documentation and download information is available at www.clawpack.org/geoclaw.

Published by Elsevier Ltd.

1. Introduction

Many geophysical flow or wave propagation problems take place over very large spatial domains, for which detailed three-dimensional modeling of the fluid dynamics is not an efficient option. Fortunately, two-dimensional depth-averaged equations such as the shallow water equations often provide models that are sufficiently accurate for many applications. Even with two-dimensional models, however, it is often necessary to use adaptive mesh refinement (AMR) techniques in order to concentrate grid cells in regions of interest, and to follow such regions as the flow evolves. This is often the only efficient way to obtain results that have sufficient spatial resolution where needed without undue refinement elsewhere, such as regions the flow or wave has not yet reached or points distant from the study area.

We will briefly describe and illustrate the use of GeoClaw, an open source research code that uses high-resolution finite volume methods together with adaptive mesh refinement to tackle geophysical flow problems. In particular, this code has recently been used together with the shallow water equations to model tsunamis and dam-break floods. In Section 7 we give a brief illustration of each. For other geophysical flow problems it may be necessary to replace the shallow water equations by a different set of depth-averaged equations. For example, in modeling landslides, debris flows, or lahars, it is necessary to incorporate terms modeling internal stress or pore pressure (e.g. [13,41]). The software is written in a manner that allows such extensions.

GeoClaw is based on the Clawpack software and is incorporated as a part of the general Clawpack distribution [30]. Clawpack (Conservation Laws Package) is an open source software package that has been under development since 1994 and is widely used for both teaching and research purposes. It is designed to solve hyperbolic systems of partial differential equations (PDEs) in one, two, and three space dimensions. This class of PDEs generally models wave propagation or fluid transport, and a wide variety of physical problems give rise to mathematical models of hyperbolic form, including for example compressible gas dynamics, linear and nonlinear acoustics, and elastic wave propagation. The theory of nonlinear hyperbolic systems and a variety of applications are described in [27], which also describes in detail the high-resolution finite volume methods implemented in Clawpack. Nearly all of the examples given in this text are available as working examples via the Clawpack website.

Clawpack is written in a formulation that allows the user to specify the system of equations being solved by providing a "Riemann solver" as described in Section 3. The software incorporates a general form of AMR as reviewed briefly in Section 4, in a manner that is easy to apply to many hyperbolic problems. However, there are several difficulties that arise when solving depth-averaged equations over realistic topography or bathymetry that required some substantial modifications to the general

* Corresponding author at: US Geological Survey, 1300 SE Cardinal Ct. #100, Vancouver, WA 98683, USA. Tel.: +1 360 993 8932.
E-mail address: dave.jorge@gmail.com (D.L. George).

approach taken in Clawpack. The GeoClaw variant of the code provides an implementation specific to such problems.

In particular, this code addresses the following issues:

- The flow takes place over topography or bathymetry that may be specified via multiple data sets covering overlapping regions at different resolutions. (Henceforth we will generally use the term topography to refer also to bathymetry.)
- Some problems can be tackled on purely Cartesian grids, but many applications require using longitude–latitude grids on the earth's surface.
- The flow is of bounded extent; the depth goes to zero at the margins and the "wet–dry interface" is a moving boundary that must be captured as part of the flow. This is handled by allowing the fluid depth to be zero in some grid cells ("dry cells"). Cells can change dynamically between wet and dry to model evolving flows or inundation, and AMR can be used to provide sufficient resolution of the shoreline or margin.
- There often exist nontrivial steady states (such as an ocean at rest) that should be maintained exactly. Often the desired flow or wave propagation is a small perturbation of this steady state, as in tsunamis. For finite volume methods that conserve mass by using the depth as a primary variable, this requires the use of a "well-balanced" numerical method as discussed in Section 3.

These issues and the algorithms in GeoClaw are discussed in more detail elsewhere [17,18,21,32,33] and here we give only a brief summary of some key aspects of the numerical algorithms (in Section 3) and the AMR procedure (in Section 4).

The computational core of GeoClaw is written in Fortran, but a user interface written in Python is provided to simplify the setup of a single run, or of a series of runs as is often required for parameter studies, sensitivity studies, or probabilistic assessments of hazards. Python and Matlab plotting tools are also provided for viewing the results in various forms, either on the dynamically changing set of adaptive grids or on a set of fixed grids, or in other forms such as gauge plots of depth vs. time at fixed spatial locations. Some of these software tools are described briefly in Section 6, and more details can be found in the on-line documentation [31].

2. Depth-averaged mathematical models

The simplest depth-averaged set of fluid equations in two lateral space dimensions are the shallow water equations

$$h_t + (hu)_x + (hv)_y = 0,$$
$$(hu)_t + \left(hu^2 + \frac{1}{2}gh^2\right)_x + (huv)_y = -ghB_x - Du,$$
$$(hv)_t + (huv)_x + \left(hv^2 + \frac{1}{2}gh^2\right)_y = -ghB_y - Dv,$$
(1)

where $u(x,y,t)$ and $v(x,y,t)$ are the depth-averaged velocities in the two horizontal directions, $B(x,y,t)$ is the topography or bathymetry, and $D = D(h,u,v)$ is the drag coefficient. Coriolis terms can also be added to the momentum equations. Eq. (1) have the form

$$q_t + f_1(q)_x + f_2(q)_y = \psi(q,x,y),$$
(2)

where $q = (h,hu,hv)$ is the vector consisting of the depth and momentum of the fluid. In the absence of bathymetry ($B \equiv$ constant, so $B_x = B_y = 0$) and drag ($D \equiv 0$), the source terms would be zero ($\psi \equiv 0$) and these equations would express the conservation of mass and horizontal momentum. We use conservative finite volume methods that in general conserve mass to machine precision (since there is no source term in the mass equation) and would also

conserve momentum in the absence of source terms. This is true even when AMR is applied, with the exception of cells that intersect the coastline, as discussed further in Section 4.

Note that for an ocean at rest, in which $h(x,t) + B(x,y) \equiv 0$ (sea level) in all wet cells, the topography source terms exactly cancel the derivatives of the hydrostatic pressure $\frac{1}{2}gh^2$. Maintaining this balance numerically is critical and is discussed in Section 3. The drag term could have many forms; for the experiments reported here we use

$$D = \frac{gM^2\sqrt{(u^2 + v^2)}}{h^{5/3}},$$
(3)

where M is the Manning coefficient, which we take to be 0.025. (Typical values for the Manning coefficient for a given substrate are empirically based. See [10] for a description and examples of values used in various applications.)

Most tsunamis are generated by motion of the sea floor due to an earthquake or submarine landslide, setting the entire water column in motion. The wave length is generally very long compared to the depth of the ocean, and under these conditions the shallow water equations (1) are generally appropriate. This has been confirmed in comparisons done by many groups (e.g. [50,25,34,44]), although in some cases it is believed that dispersive terms may need to be included (e.g. [22,43]), particularly when modeling tsunamis generated by submarine landslides, which typically have short wavelengths (e.g. [35,48]). In Section 7 we illustrate the use of GeoClaw for tsunami modeling using the shallow water equations. Adding dispersive terms would generally require the use of implicit time stepping algorithms, which are not yet implemented in GeoClaw. Development of an implicit version of the AMR routines in Clawpack is a current project and this may be possible in the future.

For other applications it is less clear that the classical shallow water equations are sufficient. For shallow flow on steep terrain, such as following a dam break for example, vertical acceleration terms may need to be added to improve the model. However, the simple equations (1) are often still used for many practical problems and can give fairly accurate results. In Section 7.3 we display some dam-break results from [19]. Some possible extensions to other depth-averaged systems of equations are mentioned in Section 8.

3. Numerical methods

The algorithms used in GeoClaw are described in detail elsewhere; see in particular [33]. Here we only give a brief summary with pointers to other sources for further reading. GeoClaw is based on Clawpack, which provides a general implementation of "wave-propagation algorithms", a class of high-resolution finite volume methods in which each grid cell is viewed as a volume over which cell averages of the solution variables q are computed. Logically rectangular grids are used and Q_{ij}^n denotes the cell average in cell (i,j) at time t_n. In each time step the cell averages are updated by waves propagating into the grid cell from each cell edge. These are Godunov-type methods in which the waves are computed by solving a "Riemann problem" at each cell edge. The Riemann problem is an initial value problem using the shallow water equations together with piecewise constant data determined by the cell averages of the dependent variables and topography on each side of the interface. The advantage of Godunov-type methods is that they provide a robust approach to solving problems with discontinuous solutions, in particular shock waves that generally arise in the solution to nonlinear hyperbolic equations. In the shallow water equations, shocks are "hydraulic jumps" or "bores", as often arise in practical flow problems. The Riemann problem defined at each cell

interface allows for shock waves in each Riemann solution and "approximate Riemann solvers" are used that rapidly produce robust solutions as a building block for the numerical method. Correction terms are also incorporated so that the computed solution is second-order accurate in smooth regions of the flow.

GeoClaw employs a variant of the f-wave formulation, described in [18], which allows the topography source terms to be directly incorporated into the Riemann problem. The f-wave formulation of the wave-propagation algorithms was originally presented for the shallow water equations in [4]. In this approach it is the difference in the *flux* normal to the cell interface that is split into propagating waves (rather than the jump in Q), but only after modifying the momentum components of the flux difference by the topography source terms. This is done in such a way that the methods are well-balanced for the ocean at rest: if the initial data is in equilibrium with zero velocities and a flat surface ($h + B =$ constant) then the modified flux difference is the zero vector, leading to zero-strength f-waves and no change to the solution. This approach to well balancing is discussed in more detail in [4,29,33] and Section 17.14 of [27].

The f-waves modify the cell averages on each side of the interface. We also solve a "transverse Riemann problem" in which the waves moving normal to the cell edge are split in the transverse direction and modify the cell averages in adjacent rows of grid cells. This improves stability and accuracy of the method and this general approach is discussed in more detail in [26] and Chapters 20–21 of [27], for example. The f-waves are also used to define correction terms modeling second derivatives normal to the interface that, together with the transverse terms, make the method second order accurate for smooth solutions. Before calculating these terms, however, wave limiters are applied to the f-waves to reduce their amplitude in regions where the solution varies rapidly. This results in a "high-resolution method" that avoids nonphysical oscillations in regions where the solution is rapidly varying. This methodology has been well developed in the context of shock-capturing for general nonlinear hyperbolic systems of equations and leads to a robust method.

Developing a Riemann solver that works robustly in the presence of dry states is particularly challenging—it must handle the case where one state in the Riemann problem is already dry as well as situations where a cell dries out as a wave recedes, and must work robustly when the topography has arbitrary jumps from one cell to the next. Details of the solver we use are given in [17–19]. Incorporation of these dry state solvers is an important aspect of GeoClaw, since we model the moving shoreline or margin of a flow implicitly as the interface between wet and dry cells. This generally means that the shoreline is represented by a stair-step pattern on a Cartesian grid. By using adaptive refinement we are able to use fine enough grids in regions of interest that this can provide sufficient resolution, but this also means that the dry-state algorithms must also function well in conjunction with AMR grids and at the interfaces between grids at different levels of refinement. This was one of the more difficult aspects of developing and debugging the GeoClaw extension.

The topography source terms (those involving B_x and B_y on the right hand side of (1)) are incorporated in the Riemann solver in order to obtain a well-balanced method and to handle the dry state problem. On the other hand, the drag source terms are handled via a fractional step approach: after each time step of the hyperbolic problem a time step is taken in which the momenta are adjusted due to the drag terms. Coriolis terms can also be incorporated in the same manner and this is included as an option in Geo-Claw, though for tsunami modeling at least this appears to be a negligible effect, both in our own experiments and elsewhere in the literature, e.g., [25].

In general Clawpack allows the solution of hyperbolic problems on any logically rectangular grid, with an arbitrary mapping function specified that maps points in computational space (a rectangular grid with uniform spacing) to the physical domain. In two space dimensions the grid cells are always assumed to be quadrilaterals with linear cell edges joining vertices that are obtained by applying the mapping function to the rectangular grid of vertices in the computational domain. On the sphere with longitude–latitude coordinates, the cell edges are great-circle geodesics and the edge lengths and cell areas must be measured on the sphere.

The wave-propagation algorithms with transverse Riemann solvers work very robustly, even on highly distorted grids or with non-smooth mapping functions. Unlike many approaches to mapped grids, we do not incorporate metric terms that depend on derivatives of the mapping function into the differential equations. Instead, we always solve Riemann problems for the original set of equations in the direction orthogonal to each cell edge. The lengths of the edges and the area of the quadrilateral cell then come into the formulas for updating cell averages. The transverse wave propagation also takes account of the fact that adjacent cell edges are not necessarily orthogonal to one another. For propagation on the earth, we use distances and areas as measured on a sphere, although in principle this could be replaced by a geoid or other surface. Currently in GeoClaw the domain choices are limited to the sphere with longitude–latitude coordinates or purely Cartesian domains, primarily because the more general routines for integrating topography data sets (see Section 5) over a general quadrilateral have not yet been developed. Longitude–latitude coordinates are suitable for modeling tsunamis on the earth, where the domain of interest is bounded away from the poles. In recent work we have also explored another class of quadrilateral grids on the sphere and present some results using AMR for a tsunami-type problem over synthetic bathymetry on the whole sphere in [5].

4. Adaptive mesh refinement

In this section we describe the patch-based mesh refinement that is used to span the orders of magnitude in spatial scales exhibited by many geophysical flow problems. For example, to go from ocean scale propagation to the resolution of small-scale coastline features in a single tsunami model, meter-scale resolution may be needed in a small subset of a domain that covers millions of square kilometers. Multiple levels of patches can be used until a sufficiently fine resolution is reached. We also give an overview of the numerical algorithms needed to initialize and remove fine grid patches, and present the organization of the time stepping procedures on the grid hierarchy.

The time step on the refined patches is chosen so that stability of the explicit finite volume method is maintained. This generally requires refining in time by the same factor as in space. For example, if the level 2 grids are refined in both x and y by a factor of 4 relative to level 1, then four time steps on all level 2 grids must be taken for each time step on level 1. The code is organized so that the time step is first taken on level 1, which covers the entire domain. Then four time steps are taken on each of the level 2 grids. In each time step it is necessary to fill in "ghost cell" values around the edges of each level 2 grid in order to provide boundary conditions for the time step. For each ghost cell, the value is either taken from a neighboring grid at the same level, if one exists, or otherwise is obtained by space–time interpolation from the values on the underlying coarse grid, which has already been advanced in time.

This same procedure is used recursively at all levels: after each time step on the level 2 grids, the required number of time steps

will be taken for all level 3 grids and so on. This AMR procedure is described in more detail in [7,33] and has been successfully used for many years in Clawpack for problems such as shock wave propagation where dozens of grid patches are used to track shock waves oblique to the grid.

The application to tsunami modeling prompted the addition of a new feature to the code: the capability of specifying anisotropic refinement in time, in which the time step from one level to the next may be refined by a different factor than the refinement in space. This is crucial for problems where very fine grids are used only near the coast of an ocean, since in the shallow water equations the wave speed is given by $\sqrt{gh}$. In an ocean with a maximum depth of 4000 m, say, this gives a wave speed of 200 m/s (and in some regions the maximum ocean depth is much greater). If a fine grid level covers only portions of the continental shelf with a maximum depth of 100 m, say, then the maximum wave speed on this level is roughly 32 m/s. Hence the refinement factor in time could be up to 6 times smaller than the spatial refinement factor on this level. Since the bulk of the computational work is often on the finest grids, this can make a substantial difference in computing time.

Grids are refined by flagging cells where the resolution is insufficient and then clustering the flagged cells into refinement patches. Flagging is done either using an error estimate (Richardson extrapolation), by examining gradients of the solution (which will detect where the largest waves are), or for the tsunami application simply by flagging cells where the surface elevation is perturbed from sea level above a specified level. In addition, it is possible to specify rectangular regions where a certain level of resolution is required. This can be used to insure that particular portions of a coastline are always refined to a resolution of meters whereas the deep ocean uses a mesh width of many kilometers. These routines are all part of the GeoClaw software, controlled by user-specified tolerances along with optional user-specified regions in space and time where a minimum and maximum allowable level refinement is specified. Regardless of which method (or combination of methods) is used to control the refinement criteria, the result is a set of flagged cells needing to be covered by finer grids.

Using heuristics from the pattern recognition literature [8], these flagged cells are clustered into grid patches that are *efficient*, in the sense that the grids do not contain too many unflagged cells (which would be wasteful), while also not introducing too many separate patches (since there is boundary overhead associated with each fine grid patch). The grids also should obey a *proper nesting* criterion—a grid patch at level 4 should be surrounded by a level 3 patch, and not border directly on level 2 patches. Figs. 3 and 4 show several frames from a 5 level computation. In this example the grids were refined by a factor of 4 in going from each level to the next (hence a total refinement factor of $4^4 = 256$ in each direction from coarsest to finest grids).

Every few timesteps the features in the solution needing refinement will have moved, and the grid patches should move too. The grids do not actually *move*; rather, at discrete times new grid patches are created and their solution is interpolated from the finest previously existing grids, which are then removed. This interpolation step must be done carefully. For example, a constant sea level should be maintained even in the presence of variable bathymetry so that no waves are generated solely from grid refinement. This is accomplished by interpolating the surface elevation $h + B$ for coarser grids and then computing the depth h in the fine cells by subtracting the fine cell value of topography B. This maintains conservation of mass provided that the fine and coarse topography are *consistent*, in the sense that the topography value used in a coarse cell should be the average of the values in all fine cells that cover this cell. This is ensured by computing exact integrals of a single piecewise bilinear representation of the topography, as described further in the next section.

Similarly when a grid is removed, the coarse grid solution underneath it should be the volume-weighted average of the fine grid cells it contained so that mass is not lost or gained. Most of the time these numerical procedures are straightforward, but there are difficulties associated with the wet–dry interfaces. A coarse cell that covers a shoreline region will be either wet or dry, depending on the level of the averaged topography. Suppose it is dry, for example. When the cell is refined, typically some of the fine cells will have to be initialized with nonzero depth in order to represent the shoreline and to maintain the constant sea level required before a wave arrives. Hence it is essential that water be introduced (mass increased) in this situation. These subtleties are described more fully in [33].

5. Topography data sets

To use GeoClaw the user must provide one or more files that specify the topography for the terrain on which the flow evolves. Each topography data set specifies the z coordinate (relative to sea level, for example) at a set of points on a rectangular grid (a longitude–latitude grid if this coordinate system is being used). Several different formats are allowed (see the documentation [31]).

Appropriate data sets for many regions of the earth are available online, for example from the National Geophysical Data Center (NGDC) [39]. A few data sets for test problems are available in the GeoClaw topographic database [16], and more will be added in the future. The test problems in GeoClaw include Python scripts to automatically download this data as needed. Some example instead use synthetic data (for example the tsunami model presented in Section 7.1) and again a Python script is provided to create this.

Some applications also require a dataset that describes the motion of the topography relative to an initial topography, for example if seafloor motion resulting from an earthquake or submarine landslide is used to generate a tsunami. In this case one or more files must also be provided to specify the relative displacement at one or more times.

Often more than one topography file is used at different resolutions. For example, in a tsunami simulation a large region of the ocean may be modeled, for which a fairly coarse resolution such as the 10-min or 4-min ETOPO2 data available from NGDC is sufficient. These have resolutions of roughly 18.5 km or 7.5 km, respectively in each direction near the equator. Since the wavelength of tsunami waves is typically 10 s–100 s of km this is sufficient for modeling propagation across the ocean. However, it is not sufficient for modeling inundation of specific regions along the coast, and so this data must generally be supplemented with one or topography files at much higher resolution over small regions.

In GeoClaw, an arbitrary number of topography files can be provided for a single run and at each point in space the topography will be determined from the dataset covering this point at the finest resolution. The user should be aware, however, that this means there will generally be discontinuities in the effective topography along the boundaries of fine scale datasets.

In the same way that h_{ij}^n represents the cell average of the fluid depth for a finite volume method, we also need a cell average B_{ij} of the topography in each grid cell. Topography data sets generally give the pointwise value of $B(x,y)$ on a grid of spatial locations. To convert this into cell averages, we construct a piecewise bilinear function that interpolates the pointwise values and then compute the exact integral of this interpolating function over a grid cell to obtain B_{ij}. This is easy to do if there is a single best-resolution data set in the region around a cell, but if a grid cell covers an area where two or more different data sets must be sampled then

computation of the integral is more difficult. This often happens in realistic tsunami simulations. Fine grid topography for a small region of the coast may lie entirely within one grid cell on the coarsest computational grids, for example. We have implemented this quadrature in full generality to guarantee that the topography values used are consistent between different adaptive mesh refinement levels.

6. Software tools and user interface

GeoClaw is comprised of a set of library routines written in Fortran 77 and 95, in addition to a set of Python modules called PyClaw. The Fortran library builds on the AMRClaw library of Clawpack, which was developed to apply AMR more generally to hyperbolic problems. GeoClaw replaces many of the routines in AMRClaw with new ones specifically designed for geophysical flow problems. Most of the core computation is done in the Fortran routines. Python is used to fetch and operate on the topography, setup the simulation run parameters, setup the plotting options and create plots. More details about many of the tools mentioned in this section can be found in the on-line GeoClaw documentation [31].

We use the Subversion version control software and the Trac interface as a development wiki and for its ticket system for bug tracking. These can be found via the Clawpack webpage [30].

6.1. Problem specification

GeoClaw uses a Python script to prescribe most of the input parameters. The script constructs a data object that contains values for all parameters that GeoClaw needs to run, and then writes them out to a set of ASCII files that are read into the GeoClaw Fortran code at run time. There are several reasons for taking this approach to prescribing the input files. A major advantage is that it is easier to maintain backward compatibility as Clawpack and Geo-Claw evolve. If a new feature is added that requires new input parameters, these can be added to the Fortran code and default values added to PyClaw so that old applications continue to run without change to the user's input script. It is also easier to write a flexible parser in Python than in Fortran, and the use of a Python script for setting the parameters allows the user to use loops or functions, for example to define an array of desired output times using the `linspace` command of `NumPy`. Sample input files can be viewed in the documentation (see the sections on `setrun.py` or the sample codes to accompany this paper at [6].

The Fortran code is a stand-alone code that reads the input files created by the Python script as data and handles memory allocation using a combination of Fortran 95 dynamic memory operations and a large work array that is managed by our own Fortran routines to efficiently allocate and deallocate storage needed for all of the AMR grids. The Fortran `allocate` statement is used only if the size of the work array needs to be increased during the computation, in which case it is generally doubled in size. Software such as `f2py` allows one to easily call Fortran from Python code and a future project is the ability to control time-stepping from a Python wrapper that would be able to produce plots as the computation proceeds, for example. In one space dimension the PyClaw software also includes a pure Python version of the finite volume methods with no Fortran component. This is useful as a test bed and teaching tool but runs considerably slower than the Fortran version.

6.2. Plotting

Early versions of the Clawpack software included a set of Matlab plotting routines for visualizing the results. Some specialized versions of the Matlab plotting routines were created for dealing with topographic data sets and are available in GeoClaw. Recently, however, the main development of plotting tools for Clawpack has shifted from Matlab to Python for a number of reasons. Many users of Clawpack do not have access to Matlab and it is desirable to have an open source alternative. Moreover, in the past few years substantial improvements have been made in Python plotting packages that provide quality that equals or exceeds that of Matlab graphics. For two-dimensional plots of the type shown in this paper, we use the `matplotlib` module [36].

We have developed a Python plotting module that allows the user to easily specify a set of plots to be produced for each frame of a simulation. When AMR is being used it is necessary to loop over all grids and combine the solution on each grid into a single plot. It is often desirable to combine several plots in a single figure. For example, we may want to do a pseudo-color plot of the water surface elevation using one color map while the topography in dry regions is also plotted with a different color map. Contour lines of bathymetry may be added to this along with indications of locations of tide gauges, resulting in a plot such as the ones shown in Section 7. The logic of looping over the grids is handled by the plotting module and the interface provides a mechanism for specifying a variety of different plots or combinations of plots on a single axis without the user needing to deal with the AMR data structures. Other useful tools such as codes for dealing with the topographic data sets and colormaps appropriate for these problems are also included.

There are also several ways the user can view plots coming from a simulation. There is an interactive Python module `Iplotclaw` for stepping through the frames of a simulation and producing the plots on the screen, facilitating data exploration via zooming in on features of interest, for example. Alternatively, it is easy to generate a set of hardcopy files in formats such as `png` or `jpg`, one for each figure at each time frame, together with a set of webpages designed to easily browse through the collection of plots. Webpages are automatically created to loop through all frames of each figure, creating an animation that is often extremely useful in developing a better understanding of the time-evolution of the flow. This set of webpages also simplifies the process of archiving past experiments for later viewing, or for sharing simulations with others. Examples can be viewed on the webpages that accompany this paper [6] and in the gallery of Clawpack and GeoClaw applications in the documentation. Many of these tools have been developed with the aim of encouraging users to adopt the paradigm of *reproducible research* in computational science. The approach we have taken with Clawpack is discussed in more detail in [28].

For three-dimensional surface plots we are currently investigating several options, including Mayavi [37], which is included (along with `matplotlib`) in the Enthought Python Distribution [14], and VisIt, an open source visualization package being developed at Lawrence Livermore National Laboratory [47]. VisIt provides more functionality for large scale visualization problems and is designed to work well with AMR data and distributed memory supercomputers. Development of 3D plotting tools for GeoClaw and Clawpack more generally is an on-going project.

6.3. Extending GeoClaw

An important aspect of GeoClaw is the ease at which GeoClaw can be extended to include other physics and algorithms. These extensions can be added in a number of ways, for example through modification of the Riemann solvers or by adding a source term. Different physics can be incorporated into the Riemann solver, to model problems for which the shallow water equations are not sufficient. Source terms, represented by ψ on the right hand side of Eq. (2), are used to incorporate bottom friction terms and

Coriolis terms, for example. These can be extended to model other terms, such as the wind forcing of a tropical storm to model storm surge. A fractional step procedure is used in which time steps on the homogeneous hyperbolic system are alternated with time steps on the source terms, and so the user need only supply a subroutine that takes a time step on the system $q_t = \psi(q)$.

Another aspect that users may way want to modify is the algorithm used to flag grid cells for refinement. Currently, GeoClaw uses displacement from sea level in addition to a set of fixed refinement regions that can be specified by the user. One could alternatively refine based on the momentum or speed of the fluid, for example.

The Clawpack and GeoClaw documentation contains more information on these routines and how they can be extended. A number of other extensions are currently being developed and some of these are briefly discussed in Section 8.

7. Applications

We briefly describe three applications of GeoClaw. The first is a new synthetic tsunami test problem. The second example models the 27 February 2010 earthquake in Chile as an illustration of the use of real data sets, and is included in the GeoClaw distribution. Variants of these problems are also presented in [33]. The third example is the simulation of the Malpasset dam catastrophe of 1959, which has been well studied and often used as a benchmark problem, and for this problem we give a summary of the GeoClaw results that were first presented in [19].

7.1. Synthetic tsunami test

First we present some results obtained using a synthetic data set that has been designed to illustrate the power of our adaptive refinement approach with a realistic range of spatial scales, but in a context where it is also possible to assess the accuracy of the solution. We start with a radially symmetric ocean that has a depth depending only on distance from some central point, which we take to be longitude $x_0 = 0$ and latitude $y_0 = 40°N$ (see Fig. 1(a)). Distance is measured as the great circle distance on a spherical earth by the formula

$$d(x,y;x_0,y_0) = 2R \arcsin \left((\sin(0.5(y - y_0))^2 \right.$$
$$\left. + \cos(y_0) \cos(y) \sin(0.5(x - x_0))^2 \right)^{1/2}$$

where $R = 6367.5 \times 10^6$ m is the average radius of the earth. In this formula we assume the longitude-latitude pairs (x,y) and (x_0,y_0) are

in radians to avoid the factors $\pi/180$. The bathymetry profile is shown in Fig. 1(b), where the horizontal scale is in kilometers and the vertical scale in meters. The central portion of the ocean is flat and is bounded by a continental slope and flat continental shelf, followed by a linear beach. We use a continuous piecewise cubic function whose derivative is also continuous except at r_3, the start of the beach:

$$B(d) = \begin{cases} z_1 & \text{if } d \leqslant r_1, \\ C(d) & \text{if } r_1 \leqslant d \leqslant r_2, \\ z_2 & \text{if } r_2 \leqslant d \leqslant r_3, \\ z_2 + \sigma(r - r_3) & \text{if } d \geqslant r_3, \end{cases} \tag{4}$$

where the cubic $C(d)$ is given by

$$C(d) = z_1 + \frac{(x_2 - z_1)(d - r_1)}{r_2 - r_1}\left(1 - 2\frac{d - r_2}{r_2 - r_1}\right)$$

and smoothly connects the ocean floor to the continental shelf. Here $r_1 = 1500 \times 10^3$ m is the start of the continental slope, $r_2 = 1580 \times 10^3$ m is the start of the flat continental shelf, and $r_3 = 1640 \times 10^3$ m is the start of the beach, which has slope $\sigma = 0.02$. We take $z_1 = -4000$ m for the depth of the ocean and $z_2 = -100$ m for the depth of the shelf. The initial shoreline is at 1645×10^3 m.

As a smaller scale feature we add an island on the continental shelf at one point that can be varied. The island is defined by a piecewise function of distance about a specified center point (x_1,y_1) (again using great circle distance). The center point is chosen to have distance 1600 km from the center of the ocean (hence 45 km off shore). The island is specified by $B_2(d) = 120(1 - (d/r_4)^2$ $(1 - 2(d - r_4)/r_4))$ for $d \leqslant r_4$ and zero outside this radius. Here d is the distance from (x_1,y_1) and the radius of the island is $r_4 = 30 \times 10^3$ m. The island rises from the continental shelf to a peak height of 20 m above sea level. Fig. 1(c) shows how the cross section is modified along the radial slice that passes through the center of the island.

The full bathymetry at any longitude–latitude point is thus given by

$$B(x,y) = B_1(d(x,y;x_0,y_0) + B_2(d(x,y;x_1,y_1)).$$

A Python script that can be used to generate bathymetry files with arbitrary resolution is provided in the directory for this example, which can be downloaded from [6]. Fig. 1(a) shows the entire ocean in longitude–latitude coordinates. The dashed line indicates the extent of the continental shelf. As initial data we take an ocean at rest and add a Gaussian hump of water at the center of the ocean:
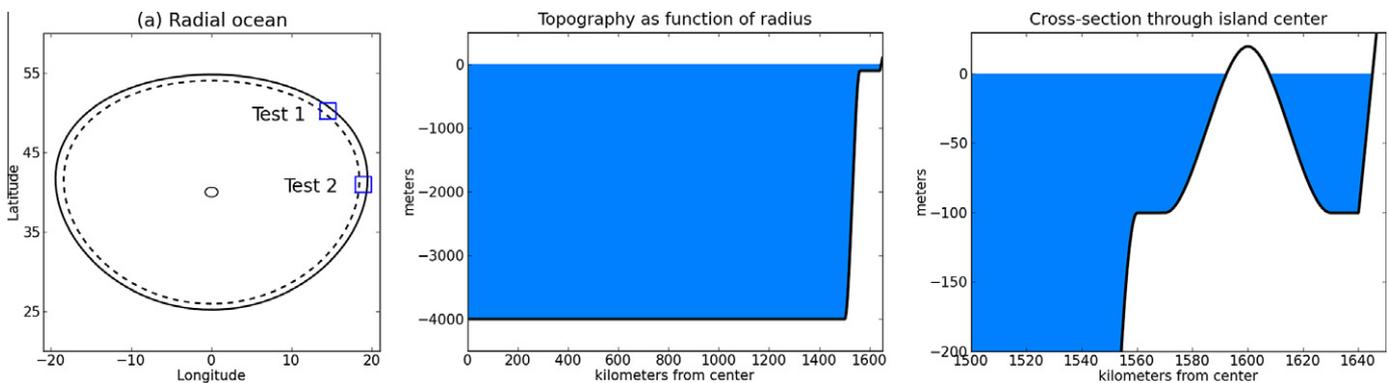

Fig. 1. (a) Geometry of the radially symmetric ocean. The outer solid curve is the position of the shoreline, with constant distance from the center when measured on the surface of a sphere. The dashed line shows the extent of the continental shelf. The boxes labelled Test 1 and Test 2 are regions where an island is located in the tests presented in the following figures. The small circle near the center shows the extent of the hump of water used as initial data. (b) The topography defined by the piecewise cubic function (4). (c) A zoom view of the topography of the continental shelf along the ray going throug the center of the island.
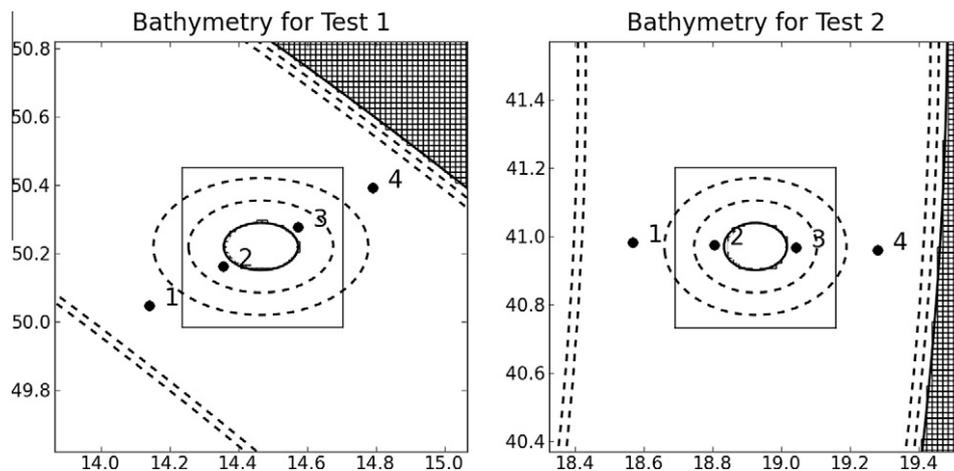
Fig. 2. Topography in regions near the island for Test 1 and Test 2. The solid contour lines are shoreline ($B = 0$) and the dashed contour lines are at elevations $B = -40, -80, -120, -160$ m. Note that the continental shelf has a uniform depth of -100 m. The level 4 grid is shown onshore. The rectangle around the island shows the level 5 grid in each computation, which is refined by an additional factor of 4 in each direction from the level 4 grids. The location of four gauges is also shown. The time history of the surface at these gauges is shown in Fig. 5.

$$h(x, y, 0) = 20 \exp(-0.5 \times 10^{-9} d(x, y; x_0, y_0)^2) - B(x, y).$$

The innermost contour on Fig. 1(a) shows the contour where the initial hump has an elevation of 2 m above sea level, 10% of its peak value.

We have performed several different runs in which the central point of the island (x_1, y_1) always has the same distance from (x_0, y_0) but is located at different angular locations. The solution to the shallow water equations with this set up should be exactly radially symmetric if there were no island. With the island the solution with different island locations should ideally be rotations of one another. This is a good test of the numerical method since the grid orientation to the shoreline near the island varies greatly depending on the its location. Here we consider two test cases: in each case an island is centered in one of the 2-degree square boxes seen in Fig. 1(a). Fig. 2 shows a close-up of the region around the island from each test case. Numbered gauge locations indicate where the solution should be identical between the two cases. The numerical solutions are shown in Figs. 3–5.

The longitude–latitude domain $[-20, 20] \times [20, 60]$ is covered with a coarse 40×40 grid, so the mesh width is one degree on this level 1 grid. Note that one degree of latitude is about 111 km and one degree longitude varies from 38 km at 60°N to 96 km at 20°N. We use 5 levels of mesh refinement, with refinement factor 4 in going from each level to the next, and hence a total refinement factor of $4^4 = 256$ from the coarsest to finest grids. The level 5 grid has a mesh width $1/256 \approx .0039$ degrees, or 434 m in the latitude direction. (More levels or higher refinement ratios could be used to refine further at particular points along the shoreline. In the tsunami computation presented in [32], for example, we used a total factor of 4096 refinement between coarsest and finest levels.)

Refinement to level 3 is allowed over the portion of the ocean that is in the direction of the study area. Refinement to levels 4 and 5 is only allowed in a small region near the island, as seen in Fig. 4.

The Gaussian initial hump spreads out into a wave that propagates radially. Fig. 3 shows the sea surface elevation at time $t = 5000$ s, for a calculation in which only 3 levels of refinement
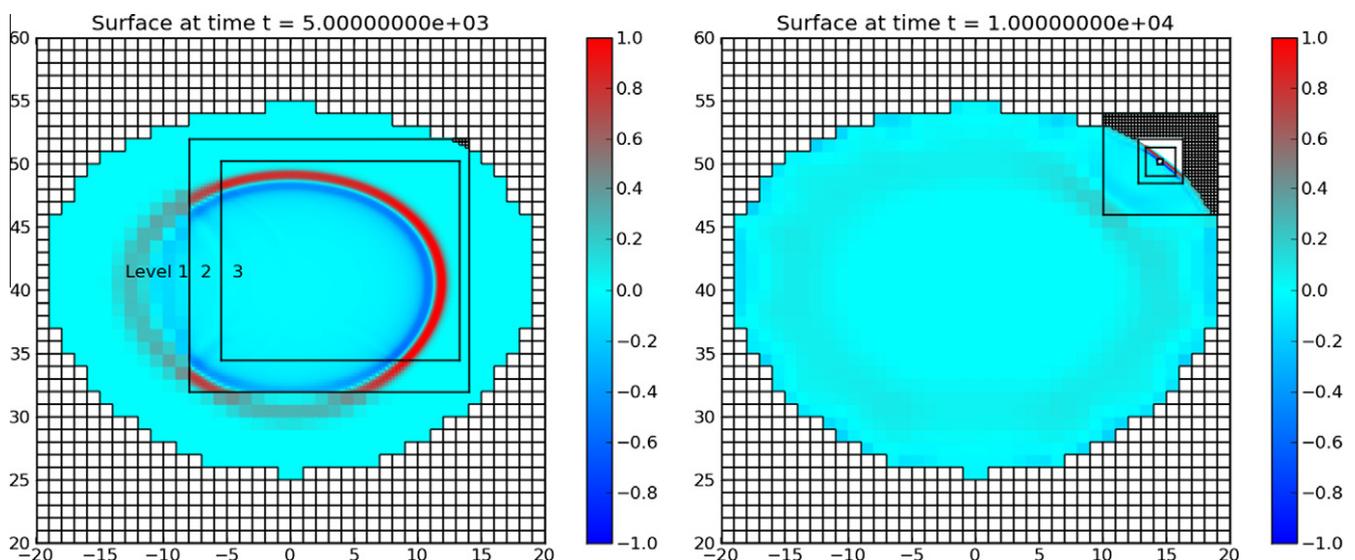

Fig. 3. Computed surface elevation for Test 1 at two different times. Left: at time $t = 5000$ s, at which point at most three refinement levels are allowed, and only in part of the domain. Right: at time $t = 10,000$, when 5 levels are allowed but only near the island, which is not visible on this scale. See Fig. 4 for a zoom of the region around the island.
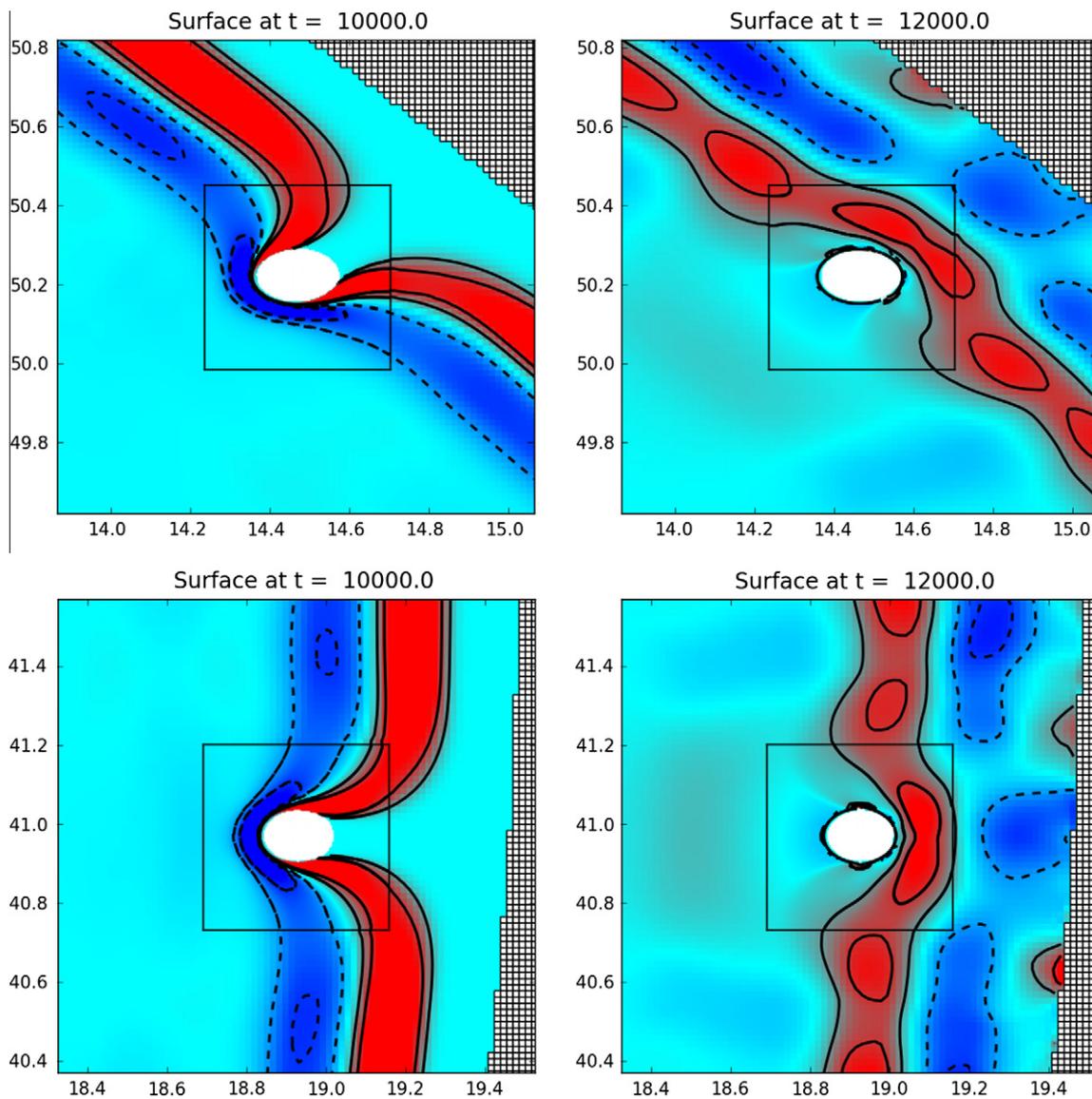
Fig. 4. Top row: Surface elevation at two times for Test 1. Bottom row: Same times for Test 2. At time *t* = 10,000 s the wave is approaching the shore. At time *t* = 12,000 the wave has reflected off the shore and is outgoing. In all cases the same contour levels are shown: the solid contours are at elevations of 0.4 m and 0.8 m above sea level, the dashed contours are at the same elevations below sea level. The inner rectangle is the interface between level 4 and level 5 grids. The level 4 grid is shown onshore. The level 5 grid is finer by a factor of 4 in each direction.

have been allowed so far, in the case where the island is located in the square indicated as Test 1 in Fig. 1(a). The edges of refinement patches are drawn and the spreading wave is poorly resolved on the coarse grid, but well resolved in the refined regions.

Note also that the calculation is done on the surface of the sphere and so the wave spreads as a circle on the sphere, but in longitude–latitude space the wave front is not circular. The wave appears to be on track to reach all points at the shore simulta- neously, as should happen, and this is confirmed in Figs. 4 and 5 which show nearly identical time histories at two locations near the shore. The top row of Fig. 4 shows three later times for an is- land located in the box labelled Test 1 in Fig. 1(a). The bottom row of this figure shows the same three times for a second test run, in which the island was located in the box labelled Test 2 in Fig. 1(a).

Fig. 5 shows solution data from the computation at four differ- ent gauges, the locations of which are shown in Fig. 2, on the radial line from the center of the ocean that passes through the center of the island. Gauges 1 and 2 are distance 1570 km and 1590 km from

the center, on the seaward side of the island, while Gauges 3 and 4 are distance 1610 km and 1630 km from the center of the ocean, on the lee side. Gauges 1 and 4 are in regions that are never refined beyond level 4, while Gauges 2 and 3 are with the region refined to level 5. Each figure shows two curves for each gauge, one from Test 1 (solid lines) and one from Test 2 (dashed lines). In principle these should lie on top of each other and in fact the agreement is quite good.

Each of these calculations (for Test 1 and Test 2) required roughly 18 min of one processor on a 32 bit, 2.26 GHz MacBook Pro laptop computer. Approximately 55 million grid cells were ad- vanced in time over the entire computation, of which roughly 14 M were on level 3, 28 M on level 4, and 11 M on level 5. Levels 1 and 2 combined accounted for less than 1 M.

7.2. The 27 February 2010 tsunami

The GeoClaw code has been used to model several historical tsunamis using bathymetry and topography data sets obtained
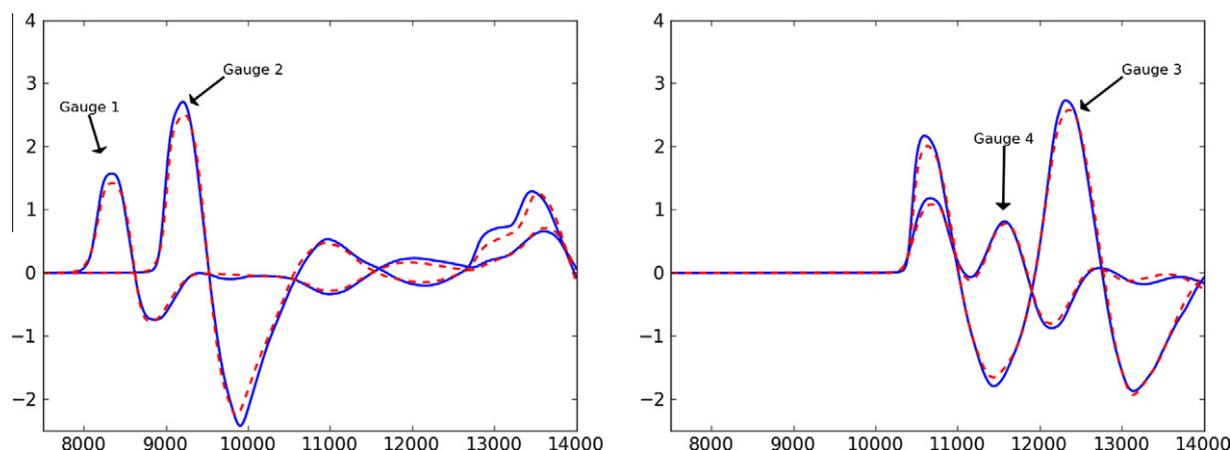
Fig. 5. Comparison of gauge output from Test 1 and Test 2, showing the surface elevation (vertical axis, (m)) as a function of time (horizontal axis, (s)) for the gauges shown in Fig. 2. In each case the solid blue curve is from Test 1 and the dashed red curve is from Test 2. (For interpretation of the references to colour in this figure legend, the reader is referred to the web version of this article.)

from NDGC [39] and other sources. Some simulations of the 26 December 2004 tsunami in the Indian Ocean following the Sumatra–Andaman earthquake are presented in [21,32] and several other studies are under way to be published elsewhere. See [6] or [31] for links to some animations.

Here we present some results for the 27 February 2010 Chile event. This example is included in GeoClaw as a sample to illustrate the use of topography data sets. In this case we use 10-min ETOPO2 topography from NGDC [39]. The seafloor motion is generated using the Okada model [40], which translates earthquake parameters taken from [45] into seafloor deformation, using a general Python function implementing the Okada model that is included in GeoClaw.

It should be noted that there are many uncertainties in the data used for tsunami modeling. In particular, the motion of the seafloor that generates the tsunami is generally not well determined. Even after seismologists use a multitude of seismic signal measurements to perform source inversion and determine the slip of the earthquake, this typically takes place many km beneath the seafloor. The seafloor displacement is dependent on the subsurface geologic structure and is only approximated by the Okada model, which assumes an isotropic material in a half-space. One use of tsunami modeling is to perform source inversion directly from measurements of the tsunami to estimate directly the seafloor displacements. This is the primary purpose of the DART buoys (Deep-ocean Assessment and Reporting of Tsunamis), and other devises that measure the pressure at the seafloor in deep water and make possible the early estimation of a tsunami's magnitude and destructive potential [38]. However, the paucity of such data makes it difficult to obtain detailed reconstructions of the seafloor displacement.

Fig. 6 shows four frames from a 3 level simulation. Level 1 has cell size 2 degrees. Refinement factors of 2 and 6 are used, so the finest grid has cell size of 10′ and matches the topography data. The dot labelled 32412 shows the position of DART buoy 32412 [11], which collected data during the event. Fig. 7 shows this data together some GeoClaw modeling results. The 3 level simulation is as described above. The uniform grid simulation was performed on a 360 × 360 grid with 10′ resolution, corresponding to the finest level of the 3 level run. The 3 level results lie on top of the uniform grid results at early times, as one would hope to see. At later times the 3 level simulation is less accurate because the region near the DART buoy is no longer refined once the main tsunami wave has moved past it. Fig. 7 also shows results obtained with a 4 level simulation using refinement factors 2, 6, and 8, so that the finest has

1.25′ resolution. With this resolution the leading peak is captured better and the amplitude of the primary wave is well estimated.

Note that there is very little evidence of spurious reflected waves at the refinement boundaries in this figure (or in the figures from the previous example). This is true in general with the AMR approach used in Clawpack. Moreover, for problems where the computational domain does not cover the full ocean (such as in Fig. 6), it is important that the method does not generate spurious numerical reflections at these outflow boundaries. The Godunov-type wave-propagation algorithms do a very good job of providing non-reflecting boundary conditions simply by using constant extrapolation into ghost cells at the domain boundaries: the values in interior cells adjacent to the boundaries are copied into ghost cells. Then solving the Riemann problems at the interfaces along the boundaries results in zero-strength waves propagating into the domain, and hence no apparent reflection of the out-going waves.

The 3-level computation ran in about 1.5 min on a 64 bit, 2.26 GHz MacBook Pro laptop, advancing 21 million grid cells. By contrast, the 360 × 360 uniform grid computation on this domain (at the resolution of the finest AMR grid) required about 8 min of computer time, advancing 137 million grid cells.

The advantage of AMR is clear, even for this problem where we are not zooming in on regions of the coast to model inundation.

The uniform grid calculation exhibits a larger number of "cells advanced per second of computation" (285 K vs. 233 K), due to the overhead of adaptive refinement. This overhead is greater in GeoClaw than normally found in Clawpack because of the need to recompute the topography in each grid cell each regridding time. In this calculation we regrid every 3 time steps to insure waves do not leave refinement patches between regridding. In the future we hope to improve the efficiency of regridding the topography.

7.3. Riverine and overland flooding

The shallow water equations are often used to model riverine or overland flooding problems, such as those due to dam/levee breaches (e.g. [23,46,2]). For flooding problems in rugged mountainous terrain, where rapidly varying contours in the topography create highly irregular domains, adaptive mesh refinement can be a valuable tool because the optimal grid resolution is highly spatially and temporally dependent yet unpredictable before doing the computation. A common approach for modeling floods in complicated topographic regions is to use static irregular meshes that
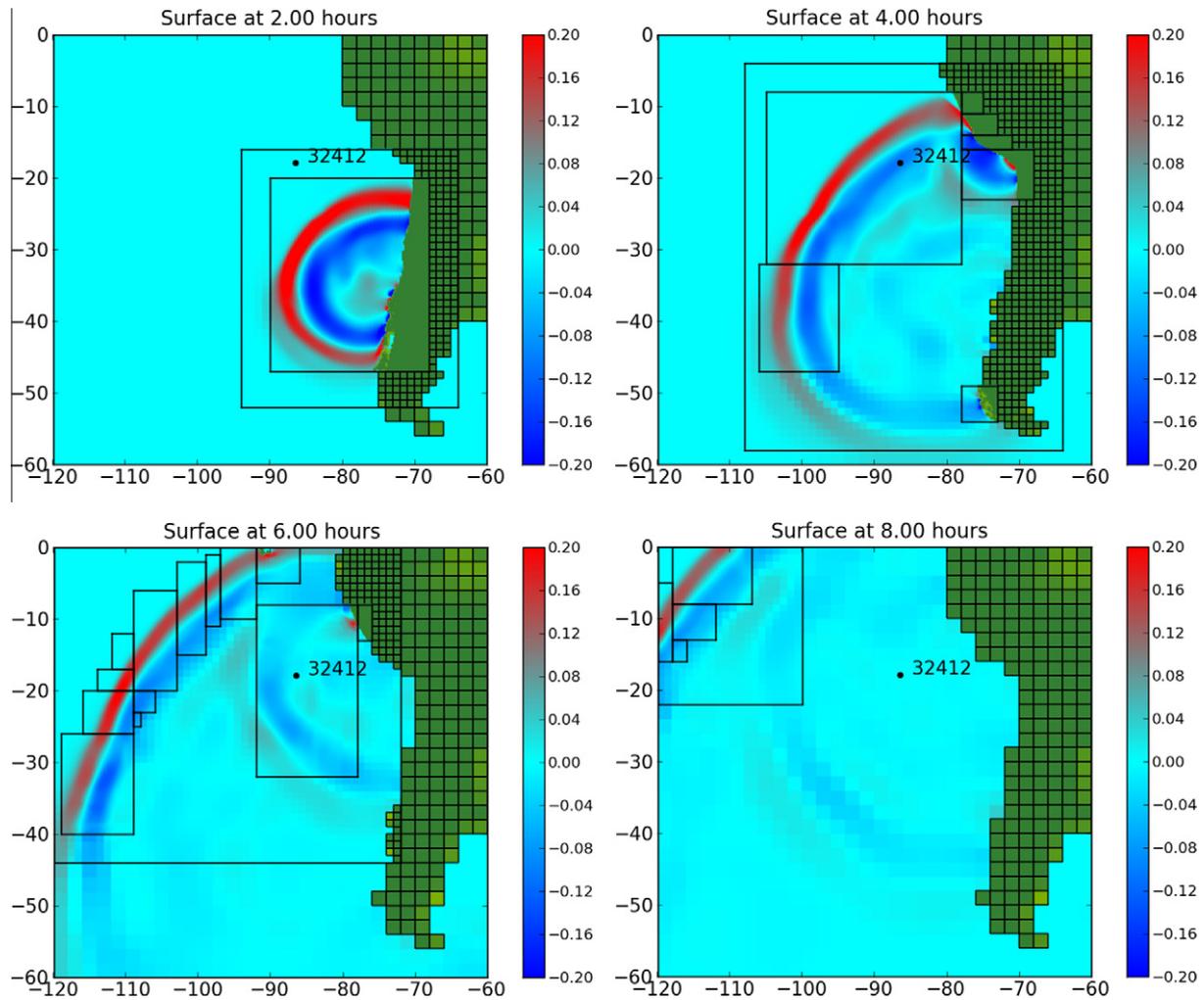
Fig. 6. Four frames from a 3 level simulation of the 27 February 2010 Chile event. The location of DART buoy 32412 is also indicated, for which the time history is shown in Fig. 7. Note the reflection from the Gallapagos near the equator at 6 h.
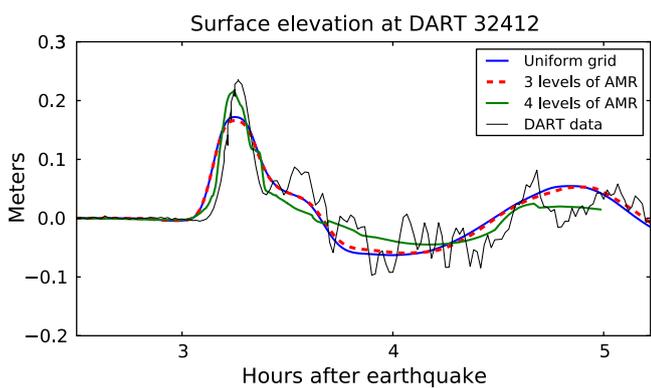

Fig. 7. Time history at DART buoy 32412, together with computational results from three GeoClaw runs as described in the text.

are fit to the topography in some fashion (e.g. [46]). However, by using adaptive mesh refinement, uniform rectangular grids can be used for such problems, resolving the flood on an evolving patchwork of finer grids that advance with the flood waves through topography. This makes it much simpler to set up a general problem.

We have tested GeoClaw in this context by modeling the historic Malpasset dam-break flood, which occurred in southern France in 1959 (see [19]). This thin-arch dam failed suddenly and explosively, sending a roughly 60 m deep flood wave into the winding ravine below, eventually inundating the Reyran River Valley. This disaster has served as a valuable test case for code validation due to the extensive field data, such as high water marks, collected after the event. For this problem we used a 6.47 km east–west (x-direction) by 16.58 km north–south (y-direction), rectangular grid. The coarsest level 1 grid was 16 by 40 grid cells respectively ($\Delta x \times \Delta y \approx 404.4$ m $\times$ 414.5 m). Level 2, level 3 and level 4 grids were then used to refine the flowing water, with refinement ratios of 8, 4 and 4, yielding ≈ 3 m $\times$ 3 m grid cells on the finest level. Some snapshots from the simulation are shown in Fig. 8. The maximum water depth computed by GeoClaw at various points was compared to other codes and empirical field and model data, shown in Fig. 9. A detailed explanation of this test problem and comparison can be found in [19].

8. Conclusions and future plans

The GeoClaw software project grew out of the TsunamiClaw code developed by one of the authors in his 2006 PhD thesis [17], which itself grew out of Clawpack. It has undergone several more years of development and testing, primarily on tsunami simulation. The version recently released with Clawpack 4.5 (in July, 2010) is fairly robust and stable, but will continue to be developed
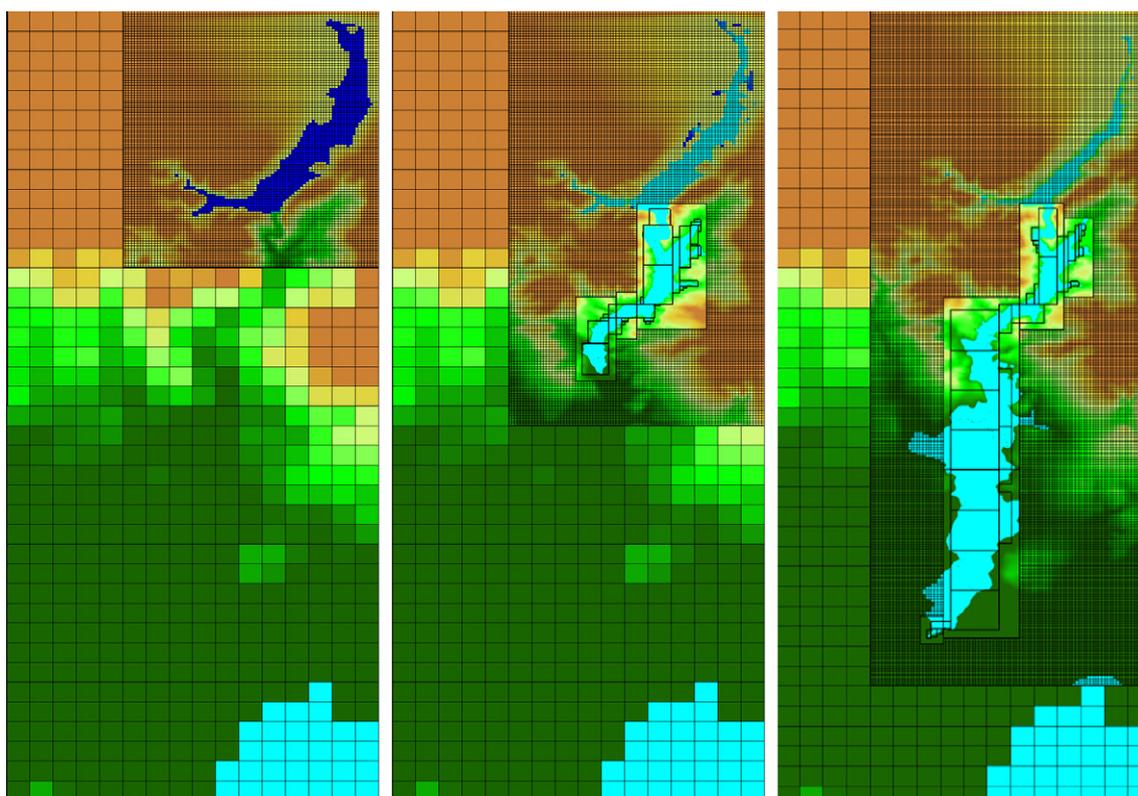
Fig. 8. A GeoClaw simulation of the Malpasset dam-break flood from [19]. Initial and later times are shown from left to right. A very coarse level 1 grid is used where the flood has yet to arrive. The reservoir in the northeast corner (upper right) is resolved on a level 2 grid. Level 3 and 4 grids surround and evolve with the flood as it winds down a ravine, eventually entering the Reyran River Valley. Individual level 3 and 4 grids are outlined; their grid lines are omitted for clarity.
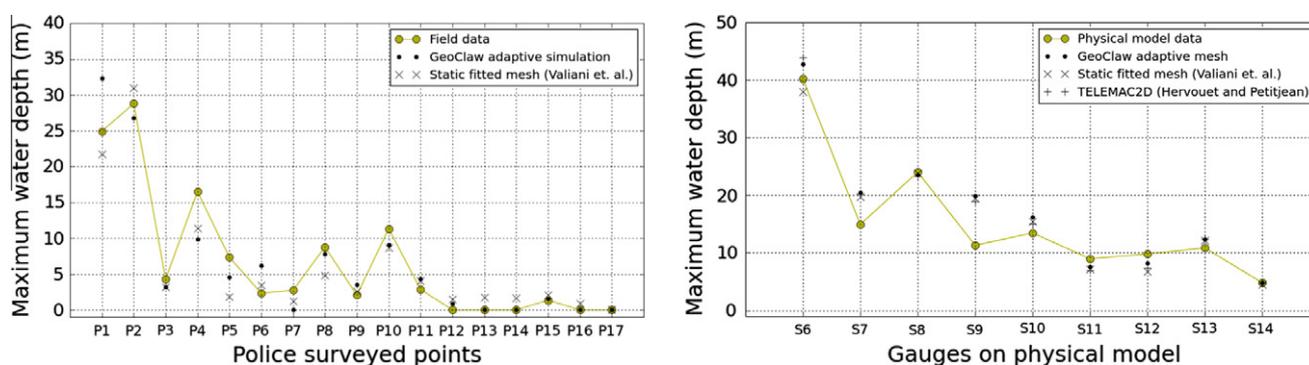

Fig. 9. Comparison of the maximum water depths produced by a GeoClaw simulation from [19] with those presented by other authors [46,23] using static topography-fit irregular meshes. Simulation results are compared with field data for high-water marks collected after the flood at 17 surveyed points (left), and with a physical scale-model experiment, where the maximum water level was recorded by electronic gauges at 12 locations (right). Depths not computed by GeoClaw are estimated by subtracting interpolated topography from the reported surface elevations. Figures are adapted from [19], where total surface elevations are shown.

and improved in the future. We are also incorporating OpenMP into the code to take advantage of multi-core shared memory computers.

A number of on-going projects by the authors make use of this software. We are currently developing depth-averaged models for two-phase flows consisting of granular-fluid mixtures, applicable to debris-flow floods and volcanic lahars or mudslides (e.g. [20,24,12,13]). These flows often occur in rugged mountainous regions, and present many of the same difficulties as overland flooding in terms of domain geometry. The shallow water equations are also often used to model storm surge, e.g. [42,49], and we are currently investigating the use of both standard single layer shallow water equations and also a multi-layer versions of the code as a possible improvement. The multi-layer version may also be useful

for modeling tsunamis generated by submarine landslides, as done for example in [15], although the multilayer shallow water equations introduce a number of new mathematical and numerical challenges (see e.g. [1,3,9]). In the future the GeoClaw webpage and the application gallery will show some results from these new application areas. Animations and some GeoClaw code to accompany the simulations presented in this paper are available at [6].

Acknowledgments

Professorship in Applied Mathematics at the University of Washington.

References

[1] Abgrall R, Karni S. Two-layer shallow water systems: a relaxation approach. SIAM J Sci Comput 2009;31:1603–27.
[2] Alcrudo F. River valley flooding simulation, in: Vilsmeier R, Benkhaldoun F, Hanel D, (editors), Proceedings of Finite Volumes for Complex Applications II, Duisburg, Germany. Editions Hermes, Paris, 1999, p. 543–550.
[3] Audusse E. A multilayer Saint-Venant model. Disc Cont Dyn Sys B 2000;6:1–14.
[4] Bale D, LeVeque RJ, Mitran S, Rossmanith JA. A wave-propagation method for conservation laws and balance laws with spatially varying flux functions. SIAM J Sci Comput 2002;24:955–78.
[5] Berger MJ, Calhoun DA, Helzel C, LeVeque RJ. Logically rectangular finite volume methods with adaptive refinement on the sphere. Phil Trans R Soc A 2009;367:4483–96.
[6] Berger MJ, George DL, LeVeque RJ, Mandli KM. Simulations to accompany this paper, 1999. Available from: <www.clawpack.org/links/papers/awr10>.
[7] Berger MJ, LeVeque RJ. Adaptive mesh refinement using wave-propagation algorithms for hyperbolic systems. SIAM J Numer Anal 1998;35:2298–316.
[8] Berger MJ, Rigoutsos I. An algorithm for point clustering and grid generation. IEEE Trans Sys Man Cyber 1991;21:1278–86.
[9] Castro M, Garcia JA, González JM, Macias J, Parés C. Improved FVM for two-layer shallow-water models: Application to the Strait of Gibraltar. Adv Eng Soft 2007;38:386–98.
[10] Chow VT. Open Channel Hydraulics. McGraw-Hill; 1959.
[11] DART Buoy 32412. Available from: <http://www.ndbc.noaa.gov/station_page.php?station=32412>.
[12] Denlinger RP, Iverson M. Flow of variably fluidized granular masses across three-dimensional terrain: 2. Numerical predictions and experimental tests. J Geophys Res 2001;106:553–66.
[13] Denlinger RP, Iverson RM. Granular avalanches across irregular three-dimensional terrain: 1. Theory and computation. J Geophys Res 2004;109:F01014.
[14] Enthought Python Distribution. Available from: <http://www.enthought.com/products/epd.php>.
[15] Fernandez-Nieto ED, Bouchut F, Bresch D, Castro Diaz MJ, Mangeney A. A new savage-hutter type model for submarine avalanches and generated tsunami. J Comput Phys 2008;227(16):7720–54.
[16] GEOCLAW topography files. Available from: <http://www.clawpack.org/topo>.
[17] George DL. Finite volume methods and adaptive refinement for tsunami propagation and inundation. PhD thesis, University of Washington; 2006.
[18] George DL. Augmented Riemann solvers for the shallow water equations over variable topography with steady states and inundation. J Comput Phys 2008;227(6):3089–113.
[19] George DL. Adaptive finite volume methods with well-balanced Riemann solvers for modeling floods in rugged terrain: application to the Malpasset dam-break flood (France, 1959). Int J Numer Methods Fluids, 2010.
[20] George DL, Iverson RM. A two-phase debris-flow model that includes coupled evolution of volume fractions, granular dilatancy, and pore-fluid pressure. Italian Journal of Engineering, Geology and Environment, in press.
[21] George DL, LeVeque RJ. Finite volume methods and adaptive refinement for global tsunami propagation and local inundation. Sci Tsunami Haz. 2006;24(5):319–28.
[22] González FI, Kulikov YA. Tsunami dispersion observed in the deep ocean. In: Tinti S, editor. Tsunamis in the World. Advances in Natural and Technological Hazards Research, vol. 1. Kluwer Academic Publishers; 1993. p. 7–16.
[23] Hervouet JM, Petitjean A. Malpasset dam break revisited with two-dimensional computations. J Hydraul Res 1999;37:777–88. 6.
[24] Iverson RM. The physics of debris flows. Rev Geophys 1997;35(3):245–96.
[25] Kowalik Z, Knight W, Logan T, Whitmore P. Modeling of the global tsunami: Indonesian Tsunami of 26 December 2004. Sci Tsunami Haz. 2005;23(1):40–56.
[26] LeVeque RJ. Wave propagation algorithms for multi-dimensional hyperbolic systems. J Comput Phys 1997;131:327–53.
[27] LeVeque RJ. Finite Volume Methods for Hyperbolic Problems. Cambridge University Press; 2002.
[28] LeVeque RJ. Python tools for reproducible research on hyperbolic problems. Comput Sci Eng 2009;11:19–27.
[29] LeVeque RJ. A well-balanced path-integral f-wave method for hyperbolic problems with source terms. J Sci Comput 2010. doi:10.1007/s10915-010-9411-0.
[30] LeVeque RJ, Berger MJ, et al. CLAWPACK software. Available from: <http://www.clawpack.org>.
[31] LeVeque RJ, Berger MJ, George DL, et al. GEOCLAW software. Available from: <http://www.clawpack.org/geoclaw>.
[32] LeVeque RJ, George DL. High-resolution finite volume methods for the shallow water equations with bathymetry and dry states. In: Liu PL, Synolakis C, Yeh H, editors. Advanced Numerical Models for Simulating Tsunami Waves and Runup. Advances in Coastal and Ocean Engineering, vol. 10. World Scientific; 2008. p. 43–73.
[33] LeVeque RJ, George DL, Berger MJ. Tsunami modeling with adaptively refined finite volume methods. Acta Numerica 2011;20:211–89.
[34] Liu PL, Synolakis C, Yeh H, editors. Advanced Numerical Models for Simulating Tsunami Waves and Runup. Advances in Coastal and Ocean Engineering, vol. 10. World Scientific; 2008.
[35] Lynett P, Liu PL. A numerical study of submarine–landslide-generated waves and run-up. Proc R Soc Lond A 2002;458:2885–910.
[36] Matplotlib software. Available from: <http://matplotlib.sourceforge.net/>.
[37] Mayavi software. Available from: <http://code.enthought.com/projects/mayavi/>.
[38] Meinig C, Stalin SE, Nakamura AI, González F, Milburn HB. Technology developments in real-time tsunami measuring, monitoring and forecasting, OCEANS, 2005. In: Proceedings of MTS/IEEE, 2006, p. 1673–1679.
[39] National geophysical data center (NGDC) GEODAS grid translator. Available from: <http://www.ngdc.noaa.gov/mgg/gdas/gd_designagrid.html>, 2010.
[40] Okada Y. Surface deformation due to shear and tensile faults in a half-space. Bull Seism Soc Am 1985;75:1135–54.
[41] Pelanti Marica, Bouchut Francois, Mangeney Anne. A Roe-type scheme for two-phase shallow granular flows over variable topography. Math Modell Numer Anal 2008;42(5):851–85.
[42] Resio DT, Westerink JJ. Modeling the physics of storm surges. Phys Today 2008:33–8.
[43] Saito T, Matsuzawa T, Obara K, Baba T. Dispersive tsunami of the 2010 Chile earthquake recorded by the high-sampling-rate ocean-bottom pressure gauges. Geophys Res Lett 2010;37:L22303.
[44] Synolakis C, Bernard E, Titov V, Kanoghu U, Gonzalez F. Standards, criteria, and procedures for noaa evaluation of tsunami numerical models. Technical report, United States Department of Commerce, National Oceanic and Atmospheric Adminstration, Pacific Marine Environmental Laboratory, Seattle WA, 2007.
[45] USGS earthquake data. Available from: <http://earthquake.usgs.gov/earthquakes/eqinthenews/2010/us2010tfan/>.
[46] Valiani A, Caleffi V, Zanni A. Case study: Malpasset dam-break simulation using a two-dimensional finite volume method. J Hydraul Eng 2002;128(5):460–72.
[47] VisIt software, Lawrence Livermore National Laboratory. Available from: <http://www.llnl.gov/visit/>.
[48] Watts P, Grilli S, Kirby J, Fryer GJ, Tappin DR. Landslide tsunami case studies using a boussinesq model and a fully nonlinear tsunami generation model. Nat Haz Earth Sys Sci 2003;3:391–402.
[49] Westerink JJ, Luettich RA, Feyen JC, Atkinson JH, Dawson C, Roberts HJ, et al. A basin- to channel-scale unstructured grid hurricane storm surge model applied to southern louisiana. Monthly Weather Review 2008:833–55.
[50] Yeh H, Liu P, Synolakis C. (editors), Long-wave runup models. World Scientific, Friday Harbor, USA; 1995.